Application of Multipass Cell Compression to Achieve High Repetition Rate Lithium Niobate Terahertz Sources With Broadened Bandwidth

Lu-Zhen Chen, Hong-Bo Li, Dong-Liang Xie, Kai Zhang, Jing-Yin Xu, Hao-Ran Song, Hong Li, Tian-Wu Wang, and Yi Qu

***Abstract*—The performance of high-repetition-rate (e.g., MHz) 1030-nm-pumped lithium niobate ($LiNbO_3$) terahertz (THz) source is significantly influenced by pulse duration, intensity, and pump wavelength. In this study, we present the application of single-stage multipass cell (MPC) compression technology to compress 1030 nm laser pulses from 200 to 49 fs and investigate its impact on THz emission using the tilted pulse front method. The results show that the compressed 49 fs pulses significantly broaden the THz spectral bandwidth, shifting the center frequency from 0.5 to 0.84 THz and extending the cutoff frequency to 4.1 THz. Although shorter pulses have lower conversion efficiency compared with longer pulses (e.g., 200 fs), they generate a broader THz spectrum. This bandwidth improvement addresses the critical limitations of narrow bandwidth and low temporal resolution in current $LiNbO_3$-based THz scanning tunneling microscopy (THz-STM) systems. By increasing the THz bandwidth, we provide an efficient approach to achieve better temporal resolution and more affluent spectral information in THz-STM systems. This study demonstrates the potential of MPC compression technology to significantly enhance THz bandwidth in $LiNbO_3$ crystals, paving the way for more accurate material analysis, imaging, and characterization using THz-STM.**

***Index Terms*—Broadband terahertz (THz) generation in lithium niobate ($LiNbO_3$), high-repetition-rate $LiNbO_3$ THz sources, multipass cell (MPC) compression, THz scanning tunneling microscopy (THz-STM).**

Received 6 February 2025; revised 25 March 2025; accepted 20 April 2025. Date of publication 28 April 2025; date of current version 25 June 2025. This work was supported in part by the National Key Research and Development Program of China under Grant 2022YFA1203500, in part by the National Natural Science Foundation of China under Grant 62464006, Grant 12274424, Grant 62274048, Grant 62174046, Grant 62064004, and Grant 61988102, in part by the Open Fund for Innovation and Entrepreneurship of College Students under Grant RSXH20231165817X and Grant RSXH20231165808X, and in part by Guangdong Pearl River Talent Program under Grant 2021QN02Z104. *(Corresponding author: Yi Qu.)*

Lu-Zhen Chen and Dong-Liang Xie are with the Hainan Normal University, Haikou 571158, China.

Hong-Bo Li is with the Aerospace Information Research Institute, Chinese Academy of Sciences, Beijing 100094, China.

Kai Zhang, Jing-Yin Xu, Hao-Ran Song, Hong Li, and Tian-Wu Wang are with the Guangdong Provincial Key Laboratory of Terahertz Quantum Electromagnetics, GBA Branch of Aerospace Information Research Institute Chinese Academy of Sciences, Guangzhou 510700, China.

Yi Qu is with the Key Laboratory of Laser Technology and Optoelectronic Functional Materials of Hainan Province, Academician Team Innovation Center of Hainan Province, Hainan International Joint Research Center for Semiconductor Lasers, College of Physics and Electronic Engineering, Hainan Normal University, Haikou 571158, China (e-mail: quyi@hainnu.edu.cn).

Color versions of one or more figures in this article are available at https://doi.org/10.1109/TTHZ.2025.3564709.

Digital Object Identifier 10.1109/TTHZ.2025.3564709

I. Introduction

Terahertz (THz) technology has been widely applied to ultrafast optics, imaging, and materials science, driving numerous innovative experiments [1], [2], [3], [4], [5], [6], [7]. Among the most effective techniques for generating high-intensity single-cycle THz pulses, the tilted pulse front (TPF) pumping method based on lithium niobate ($LiNbO_3$) crystal plays a critical role, which is commonly used in high-repetition-rate applications, such as THz scanning tunneling microscopy (THz-STM) [8], [9]. The performance of THz pulses—including pulse intensity, repetition rate, and spectral width—is significantly influenced by the characteristics of the pump laser. Currently, the most common pump sources are titanium: sapphire (Ti: sapphire) lasers and ytterbium (Yb) doped lasers. Ti: sapphire lasers, with their short pulse durations (<100 fs) and high single-pulse energy, are widely used for generating strong-field THz sources. However, their low average power at high repetition rates limits their suitability for high-repetition-rate applications [10], [11], [12]. In contrast, Yb-doped lasers, known for their higher average power during regenerative amplification, offer significant advantages for high-repetition-rate THz sources in the MHz range [13], [14], [15]. High-repetition-rate THz source holds great importance in many fields of THz applications. For instance, high-repetition-rate THz source could provide better signal–noise ratio in traditional far-field pulsed THz imaging systems [16], [17], [18]. In addition, for near-field THz microscopies associated with a nanotip, such as THz scattering scanning near-field optical microscopy (THz s-SNOM) [19], [20] and THz-coupled THz-STM [21], [26], [29], high-repetition-rate THz source plays a critical role. In THz s-SNOM systems, various kinds of background noise significantly affect the signal analysis, making high-repetition-rate THz pulse a compulsory option for reliable THz imaging. For THz-STM application, thermal expansion of the nanotip poses a great threat to the THz-induced tunneling current, which could be efficiently repressed by using high-repetition-rate THz pulses in the MHz range. These demands for high-repetition-rate THz sources urge for innovations and improvements in this field. However, the long pulse duration in Yb-doped pumping lasers, e.g., several hundreds of femtoseconds, limits their effectiveness in generating broadband THz radiation, which is critical for applications requiring both high temporal resolution and broad spectral coverage.

Previous studies have explored the use of 1030 nm laser pulses to efficiently generate THz waves from 0.6% MgO-doped stoichiometric $LiNbO_3$ crystals. For example, Fülöp et al. [22] reported the generation of strong THz pulses with an electric field strength of 650 kV/cm and a center frequency of 0.2 THz, using a 0.01 kHz pump laser with a pulse duration of 785 fs. With increased repetition rates, Schneider et al. [23] employed a 300 kHz pump laser with an 800 fs pulse duration, achieving a THz electric field strength of 10 kV/cm and a center frequency of 0.3 THz, although the spectral width remained relatively narrow due to the large pulse duration. More recently, Kramer et al. [24] utilized a single-stage gas-filled multipass cell (MPC) compression technique to shorten the pump pulse from 700 to 70 fs, with a repetition rate of 100 kHz. This approach generated a THz electric field strength of 150 kV/cm, with a center frequency of approximately 0.6 THz and a cutoff frequency of around 2.5 THz. Their study demonstrated the potential of pulse compression technology for developing broadband, high-repetition-rate THz sources. However, due to the relatively low repetition rate and high single-pulse energy, significant crystal absorption still occurred, limiting the THz spectral range. In addition, Meyer et al. [25] employed MPC compression technology to compress laser pulses to 97 fs at a repetition rate of 13.3 MHz, producing a THz source with an electric field strength of 16.7 kV/cm and a center frequency of approximately 0.7 THz. These results highlight the challenges of achieving broader THz spectra in $LiNbO_3$ crystals at high repetition rates, particularly with respect to optimizing pulse duration and spectral width for the pump light.

In the THz-STM field, it is well known that THz acts like a transient bias linear to its near-field waveform [26]. Therefore, improving the temporal resolution urges the development of broad bandwidth THz sources with narrow electric field waveform pulsewidth. In addition, broader THz bandwidth also holds importance in surface phonon-mode studies employing THz-STM system, as more phonon modes at higher frequencies on material surfaces could be excited [27]. However, the typical THz bandwidth in current $LiNbO_3$-based THz-STM systems is only less than 2 THz [28], [29], [30], [31]. Yet, despite the progress in developing broad bandwidth $LiNbO_3$ THz sources, much broader THz spectral scope at high repetition rate is still difficult to achieve. To address these challenges, this study employs MPC nonlinear compression technology to further advance the realization of broadband THz sources under high-repetition-rate conditions.

In this study, we use a single-stage solid MPC nonlinear compression system to compress high-repetition-rate (520.8 kHz) 1030 nm laser pulses from 200 to 49 fs. By comparing the compressed 49 fs pulses and the uncompressed 200 fs pulses, we investigate the effects of these different pump pulses on the THz waves generated from a 0.6% MgO-doped stoichiometric $LiNbO_3$ crystal. The experimental results show that the 49 fs pulses produce THz waves with a significantly broader spectral width, with a cutoff frequency extending to 4.1 THz and a center frequency of 0.84 THz, while the 200 fs pulses generate

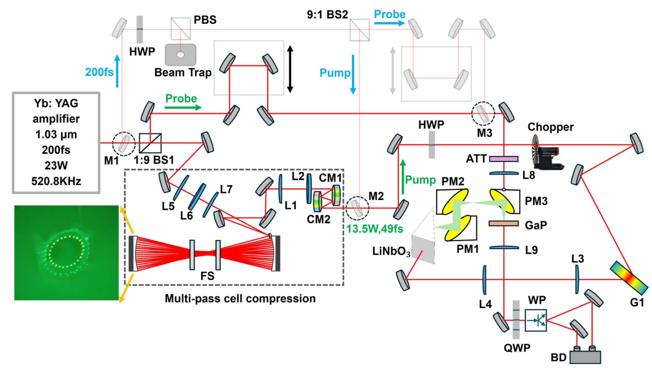

Fig. 1. Schematic diagram of the nonlinear compression and $LiNbO_3$ crystal-based THz pulse generation and electro-optic (EO) sampling detection setup. The inset shows the circular distribution of the beam spots on the cavity mirrors. The experimental setup includes a Yb solid-state amplifier laser system, a single-stage bulk MPC nonlinear compression setup, pump pulse setups of 200 and 49 fs for $LiNbO_3$ OR, and its EO sampling setup. The components are labeled as follows: *M*, movable magnetic mirror; BS, beam splitter; *L*, lens; FS, fused silica medium; CMs, chirped mirrors; HWP, half-wave plate; PBS, polarization beam splitter; *G*1, transmission grating; PM, parabolic mirror; ATT, variable attenuator; QWP, quarter-wave plate; WP, Wollaston prism; and BD, balanced photodetector.

THz waves with a center frequency of approximately 0.5 THz and a cutoff frequency of 2 THz. Through MPC nonlinear compression, it is shown that narrow pump pulses efficiently enhance the THz pulse bandwidth, providing new possibilities for the potential application of THz-STM systems [32], [33], [34].

II. Experimental Setup

In this experiment, we employed a single-stage bulk MPC nonlinear compression system to compress high-repetition-rate (520.8 kHz) laser pulses from 200 to 49 fs. Both the 200 and 49 fs pulses were used to pump an $LiNbO_3$ crystal, generating broadband THz radiation through optical rectification (OR) and TPF techniques, utilizing a 4f imaging system. The 49 fs compressed pulses generated a broader THz spectrum with enhanced time-domain resolution, which can potentially improve applications, such as high temporal resolution THz-STM imaging [33], [34].

A. MPC Experimental Setup

To achieve shorter pulse durations, we employed a single-stage bulk Herriott-type MPC for nonlinear pulse compression. The setup relies on self-phase modulation (SPM) for spectral broadening and chirped mirrors (CMs) for dispersion compensation [35], [36], [37]. As illustrated in Fig. 1, the 49 fs pulses generated by MPC compression, along with the uncompressed 200 fs pulses, served as two distinct pump sources to excite the $LiNbO_3$ crystal, generating single-cycle THz pulses.

In the experiment, we employed a Yb: YAG femtosecond amplifier (CARBIDE C20563) as the driving laser, which emitted 200 fs pulses at a wavelength of 1030 nm with an average power of 23 W and a repetition rate of 520.8 kHz. The laser's spectral width was approximately 10 nm. The MPC system consisted of two concave mirrors, each with a diameter of 50.8 mm and a radius of curvature (ROC) of 300 mm. The mirrors were coated with high-reflectivity layers featuring low group delay dispersion (GDD), optimized for wavelengths between 850 and 1100 nm. The distance between the mirrors (L) was set to 580 mm, satisfying the stability condition for a Herriott-type MPC ($0 < L < 2R$) [38], [39].

The stability of the MPC was ensured by following the principles of a stable resonator, which favors a specific light transmission mode, known as the eigenmode. Once the mirror curvature and spacing are determined, the re-entrant beam pattern after N round trips in the MPC requires the angular progression angle to satisfy the following condition:

$$C = \frac{L}{R} = 1 - \cos(\pi k/N) \tag{1}$$

where $k = 1, \ldots, N-1$, and $\xi = 2\pi k/N$ represents the angular progression of the light spots on the cavity mirrors [38], [39]. N represents the number of round trips made by the beam in the MPC. C is a constant as defined. R represents the ROC of the MPC cavity mirrors, which is 300 mm. Based on the MPC stability condition, the distance L between the MPC mirrors cannot exceed $2R$. To maintain consistent nonlinear pulse propagation characteristics over multiple round trips, the beam transmission must match the eigenmode of the MPC. The eigenmode can be analyzed using the *ABCD* transmission matrix for Gaussian transmission, and the multiple reflections within the MPC are described by the following matrix:

$$M_{\text{mpc}} = \begin{bmatrix} 1-C & L(1-C/2) \\ -2/R & 1-C \end{bmatrix}^j. \tag{2}$$

Here, the integer j is the number of reflections (52 reflections in this experiment). Simplify using $C = L/R$ defined in (1). For any integer j, applying this matrix to the Gaussian parameter q_0 should give the same value. For $j = 1$, this means

$$q_0 = \frac{(1-C)\,q_0 + RC(1-C/2)}{(-2/R)\,q_0 + 1 - C}. \tag{3}$$

The Gaussian parameter q_0 for the MPC cavity can be calculated as follows:

$$q_0 = -\frac{R}{2}\sqrt{C(C-2)}. \tag{4}$$

Based on the properties of the q parameter of a Gaussian pulse, the beam waist radius ω_0 corresponding to the linear-mode-matched beam (neglecting the effect of Kerr lensing on the MPC eigenmode) can be expressed as follows:

$$\omega_0^2 = \frac{R\lambda}{2\pi}\sqrt{C(2-C)} = \frac{R\lambda}{2\pi}\sin(\pi k/N) \tag{5}$$

where λ is the laser wavelength. Under the condition of a stable resonator (i.e., $0 < C < 2$), mode matching is feasible. Using the simple Gaussian beam equation, the beam radius on the cavity mirrors ω_m derived from

$$\omega_m^2 = \frac{R\lambda}{\pi}\sqrt{\frac{C}{2-C}} = \frac{R\lambda}{\pi}\tan(\pi k/2N). \tag{6}$$

To further broaden the input pulse spectrum, two 1-mm-thick fused silica (FS) plates were symmetrically inserted 15 mm from the center of the MPC. These media are coated with antireflection coatings. The nonlinear properties of FS make SPM the primary mechanism responsible for spectral broadening in the MPC. The laser-induced damage threshold of the MPC mirrors is typically evaluated based on two key parameters: fluence (F_m) and peak-focused intensity (I_0). These parameters are calculated using the following formulae:

$$F_m = \frac{2E}{R\lambda}\sqrt{2/C - 1} = \frac{2E}{R\lambda}\frac{1}{\tan(\pi k/N)} \tag{7}$$

$$I_0 = \frac{4P}{R\lambda}\frac{1}{\sqrt{C(2-C)}} = \frac{4P}{R\lambda}\frac{1}{\sin(\pi k/N)}. \tag{8}$$

Here, E is the pulse energy and P is the peak pulse power. The MPC mirrors were selected to operate below their damage threshold, ensuring optimal performance throughout the experiment. To achieve mode matching between the incident laser pulse and the MPC eigenmode, we employed three singlet lenses ($L5$, $L6$, and $L7$). $L5$ and $L6$ were used to control the beam size, while $L7$ adjusted the mode matching. Based on (5) and (6), the eigenmode diameter on the MPC mirrors is calculated as $2\omega_1 = 1.456$ mm, and the eigenmode diameter at the center of the MPC is $2\omega_0 = 0.266$ mm. Using (7) and (8), the fluence F_m is estimated to be approximately 4.6 mJ/cm^2, and the peak-focused intensity is about 6.9×10^{11} W/cm^2.

The incident laser pulse was coupled into and out of the MPC system via a 4-mm-wide rectangular mirror, coated with a high-reflective layer. With the aid of an infrared viewer (Electro Optic Abris-M 2000), 26 evenly distributed reflection points were observed on each cavity mirror. During each round trip, the beam advanced by four reflection points along the mirror surface, completing a total of 52 reflections. As a result, the laser pulse traversed the FS medium 52 times, inducing significant spectral broadening through SPM.

The laser pulse propagated a total distance of 0.104 m within the FS and 30.056 m in the air. To compensate for the dispersion introduced by the MPC system, CMs were employed. Dispersion compensation was achieved by reflecting the output beam three times from two mirrors with a GDD of -1000 fs^2 each, and two additional reflections from two mirrors with a GDD of -150 fs^2. This resulted in a total dispersion compensation of -3300 fs^2. The compressed pulse was subsequently characterized using a frequency-resolved optical gating (FROG) system, achieving a pulse duration of 49 fs, which closely approached the Fourier transform limit (FTL), thereby confirming the effectiveness of the MPC nonlinear compression process.

B. Generation and Detection of $LiNbO_3$ THz Source

To efficiently generate THz radiation, a 0.6% MgO-doped stoichiometric $LiNbO_3$ crystal was employed, cut into a triangular prism with a 63° apex angle. The THz radiation was produced using OR and TPF techniques, which are well-established methods for generating THz radiation in nonlinear crystals [40], [41]. A beam splitter with a 1:9 reflection-to-transmission ratio was placed before the MPC compression setup to split the incoming

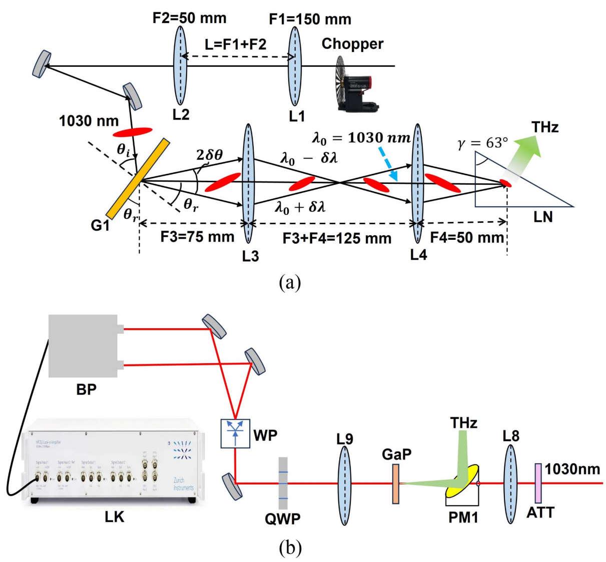

Fig. 2. Setups for the $LiNbO_3$ THz source and the EOS approach. (a) Typical $LiNbO_3$ THz source setup based on a 4f imaging system. (b) EOS setup. *L*: Lens; *G*1: Transmission grating; LN: $LiNbO_3$ crystal; ATT: Variable attenuator; PM: Parabolic mirror; QWP: Quarter-wave plate; WP: Wollaston prism; BD: Balanced photodetector; and LK: Lock-in amplifier.

beam into two parts. The 10% of the power was directed to the electro-optic sampling (EOS) detection path, while 90% was used for THz generation after MPC compression. A movable magnetic mirror was positioned near the Yb: YAG laser output to redirect the beam before it enters the MPC compression stage. After splitting, the magnetic mirror guided the compressed beam along the THz pump path and the uncompressed beam to the EOS detection path (refer to Fig. 1).

The output pulse from the MPC system passed through a half-wave plate to adjust polarization for efficient THz generation in the $LiNbO_3$ crystal. A transmission blazed grating (*G*1) with 1600 lines/mm was used, which maximizes the first-order diffraction at 1030 nm. The use of the transmission grating not only allows for a compact figuration for the optical setup but also provides a high transmission rate over 90% and a high damage threshold for strong pumping light. Due to the refractive index difference between the pump and THz pulses, momentum matching is achieved by introducing a 63° tilt angle for the pump pulse, corresponding to the apex angle of the $LiNbO_3$ crystal. This angle determines the THz radiation plane, ensuring optimal alignment for THz generation.

The efficiency of THz generation depends heavily on the proper alignment and optimization of several components in the THz generation path. The optical system was designed to accurately tilt the pump pulse wavefront and image the transmission grating precisely onto the $LiNbO_3$ crystal to maximize THz output. Parameters of the transmission grating and lenses *L*3 and *L*4 are calculated according to the $LiNbO_3$ emission theory [40]. *L*3 and *L*4 formed a 4f optical imaging system, which minimized aberrations while imaging the transmission grating onto the crystal [see Fig. 2(a)]. This system along with the transmission grating tilted the wavefront of the 1030 nm pump light in the $LiNbO_3$ crystal, ensuring efficient THz generation. In addition, two antireflection-coated lenses (*L*1 and *L*2) were used to control the pump spot size on the crystal's surface, further enhancing the THz emission. These lenses were optimized to focus the beam to a spot size of approximately 0.8 mm, defined by the full width at half maximum (FWHM). This corresponds to a spot area of approximately 5.03×10^{-3} cm^2.

To ensure that both the 200 fs and 49 fs pump pulses were under equal power conditions, the power of the 200 fs pulse was adjusted using a half-wave plate and a polarization beam splitter to match the output power of the 49 fs pulse (13.5 W), ensuring that both pump pulses delivered comparable power. Under these conditions, the single-pulse energy for both pump durations was calculated to be approximately 25.92 μJ. The corresponding peak powers were determined to be 129.6 MW for the 200 fs pulse and 529.8 MW for the 49 fs pulse. In addition, the energy densities were calculated to be 2.58×10^{10} W/cm^2 for the 200 fs pulse and 1.05×10^{11} W/cm^2 for the 49 fs pulse.

To further characterize the THz waveform and beam profile, we employed an EOS setup in conjunction with a THz camera (Swiss THz Rigi S2). A variable attenuator was placed in the detection path to control the probe beam's pulse energy. Both the THz and 1030 nm probe beams were simultaneously focused onto a 2-mm-thick GaP crystal for EOS using lens *L*8 (focal length: 150 mm) and an off-axis parabolic mirror (PM3, focal length: 50 mm). Lens *L*9 (focal length: 100 mm) was then used to collimate the converging beam from *L*8. In the pump path, a chopper operating at 611 Hz was employed for lock-in detection. A quarter-wave plate was used to convert linearly polarized light into circularly polarized light, and a Wollaston prism separated the vertical and horizontal polarization components for differential detection. The balanced photodetector measured the differential signal, which was subsequently sent to a Zurich Instruments lock-in amplifier (HF2LI) to extract the THz time-domain waveform [see Fig. 2(b)].

In this experiment, the 200 fs laser pulse before MPC compression and the 49 fs pulse after spectral broadening and dispersion compensation were used as two distinct pump sources for generating THz radiation in the $LiNbO_3$ crystal. Notably, a coherent 200 fs pulse served as the same probe beam for these two pump conditions, employing the EOS technique to measure the THz time-domain waveform. This configuration allows us to explore THz generation under different pulse durations (49 and 200 fs) and to perform a detailed comparison of the THz pulse characteristics for both pumping conditions.

III. Experimental Results and Discussion

This section presents the results of spectral broadening and pulse duration reduction achieved by compressing high-repetition-rate Yb-amplified laser pulses. By reducing the pulse duration from 200 to 49 fs, we observed significant broadening of the THz spectrum, with the compressed pulse duration approaching the FTL. The impact of pump pulse duration on the generated THz radiation was systematically investigated,

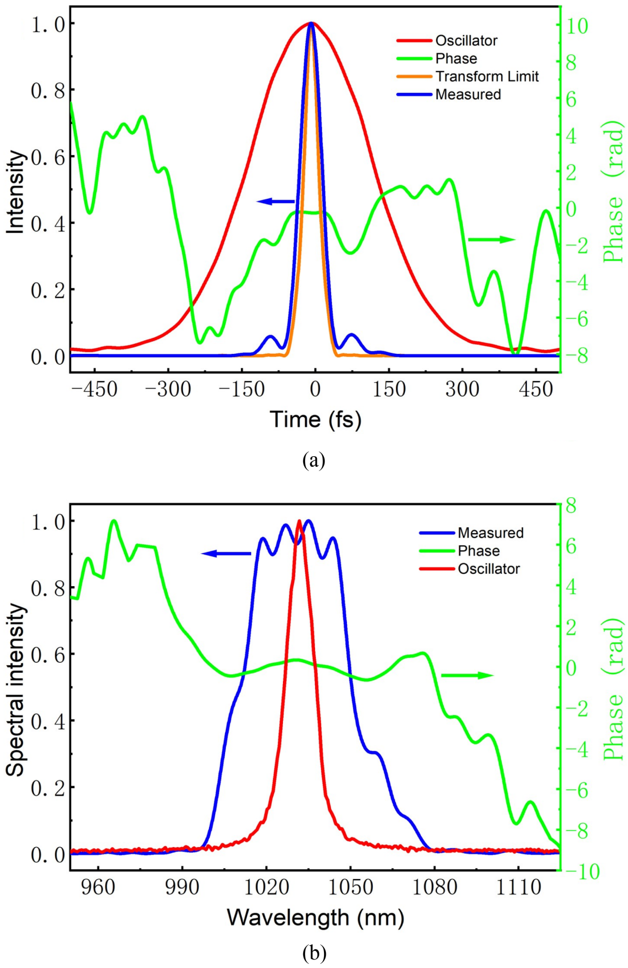

Fig. 3. Characteristics of the compressed pulse. (a) Autocorrelation traces before compression (red) and after compression (blue), along with the phase change after compression (green) and the autocorrelation measurement of the Fourier transform-limited pulse (orange). (b) Spectra before compression (red) and after compression (blue), along with the spectral phase change after compression (green).

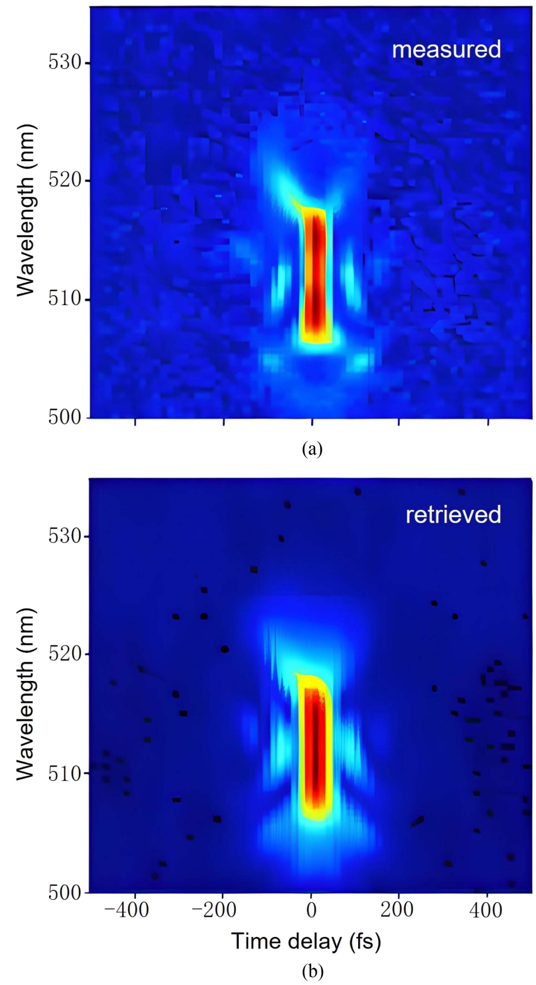

Fig. 4. (a) and (b) show the measured and retrieved FROG traces of the compressed laser pulse.

revealing that shorter pulse durations not only enhanced the spectral bandwidth but also increased both the center and cutoff frequencies of the THz emission. These findings highlight the crucial role of optimizing pump pulses to improve the performance of broadband THz sources.

A. Spectral Broadening and Recompression of the Yb-Amplified Laser System

The output power of the laser pulse after spectral broadening and recompression in the MPC system was measured using a power meter, yielding 13.5 W. This corresponds to a transmission efficiency of approximately 65% within the MPC setup, indicating effective energy transfer during the nonlinear compression process.

To characterize the compressed pulses, we employed a FROG instrument (Mesa Photonics FROG scan). Fig. 3(a) shows the autocorrelation traces of both the initial 200 fs pulse (before MPC compression) and the compressed 49 fs pulse (after MPC compression), along with the associated phase shift of the 49 fs pulse. The full width at FWHM of the compressed pulse was measured at 49 fs, which closely matches the FTL, confirming successful pulse recompression. Fig. 3(b) presents the spectra of both the initial 200 fs pulse and the compressed 49 fs pulse, along with the spectral phase corresponding to the 49 fs pulse. The spectrum broadened to approximately 40 nm (measured at half the intensity of the outer spectral peaks), representing a fourfold increase in bandwidth. The spectral peak structure shows the characteristics of SPM, confirming SPM as the primary mechanism for the observed spectral broadening. Fig. 4(a) and (b) shows the measured and retrieved FROG traces, which exhibit near symmetry, further validating the effectiveness of the nonlinear compression process and confirming that the pulse compression was close to the FTL.

To assess the preservation of beam quality after compression, we measured the M^2 factor using a Thorlabs scanning slit beam quality analyzer (BP209-VIS: 200–1100 nm). The M^2 values for the input beam before MPC compression, as shown in Fig. 5(a), were 1.30 and 1.31 for the X and Y axes, respectively, with an estimated waist relative astigmatism (ESA) of 0.34%. After compression, as shown in Fig. 5(b), the M^2 values were 1.51 and 1.40 for the X and Y axes, indicating minor degradation in beam

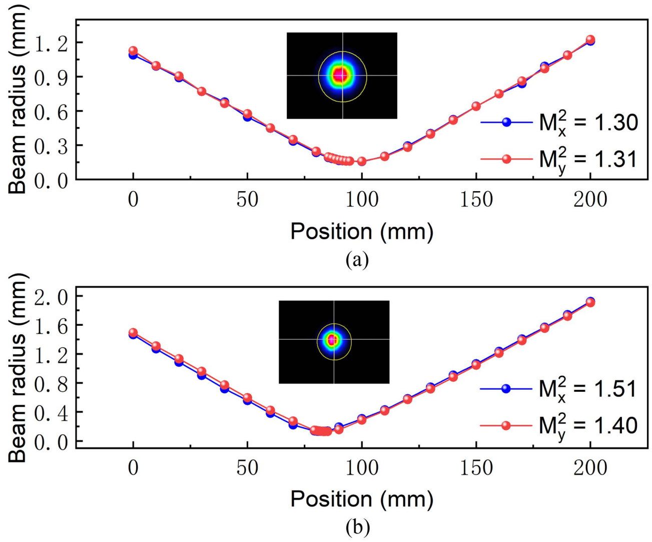

Fig. 5. Beam quality factor measurement (M^2) of the (a) input beam before MPC setup and (b) output beam along the transverse axes. The solid lines show the hyperbolic fits to the measured beam caustics.

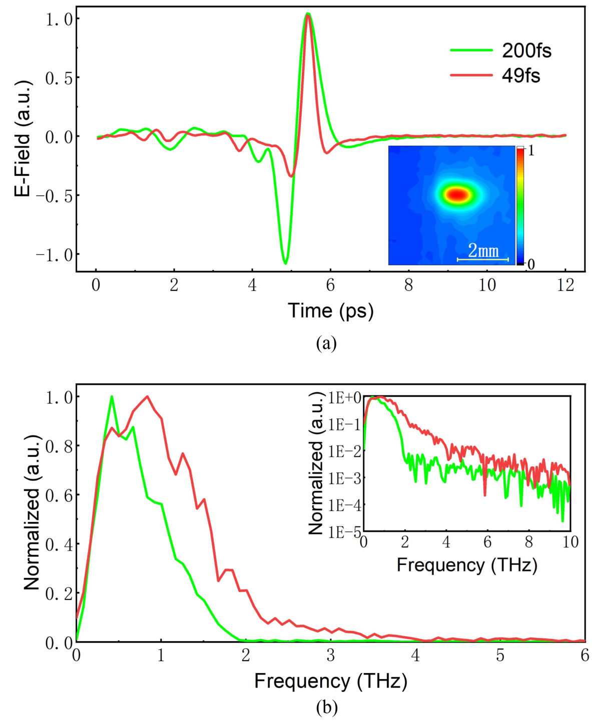

Fig. 6. Characterization of THz output results. (a) Comparison of the THz time-domain waveforms of the $LiNbO_3$ crystal under two pump conditions with pulse durations of 49 and 200 fs, with the inset showing the THz beam profile by the 49 fs pump pulse. (b) Normalized spectra comparison of the generated THz pulses.

quality. The final ESA was measured at 4.35%, which is similar to the input values. This slight increase in astigmatism is likely due to alignment errors during the M^2 measurement, rather than originating solely from the MPC compression process itself.

In this section, we demonstrated that the single-stage bulk MPC compression system successfully achieved substantial spectral broadening and pulse recompression, reducing the pulse duration from 200 to 49 fs. This compression, driven by SPM, resulted in significantly increased spectral bandwidth. The preservation of beam quality with minimal astigmatism further confirms the robustness of the MPC system.

The primary objective of achieving such ultrashort pulses is to optimize the generation of broadband THz radiation in $LiNbO_3$ crystals. Shorter pump pulses are essential for enhancing the bandwidth of the THz spectrum, and the compressed 49 fs pulse is expected to significantly improve the bandwidth performance of the $LiNbO_3$-based THz source. Therefore, this work on nonlinear compression is fundamental to achieving high-performance, broadband THz generation, which has broad implications for applications in spectroscopy, high-resolution imaging, and other THz-related fields.

B. Characterization of THz Generation Results

In this experiment, the initial 200 fs laser pulse was compressed to 49 fs using the MPC nonlinear compression system. Both 49 and 200 fs pulses at 1030 nm were used as pump sources for the $LiNbO_3$ crystal to investigate the impact of different pulse durations on the THz spectral bandwidth at a high repetition rate of 520.8 kHz. The primary goal was to highlight the advantages of using shorter pumping pulses, generated through MPC compression, in producing a broader THz spectrum from the $LiNbO_3$ crystal, especially for applications in THz-STM, which urges for broader THz bandwidth.

THz time-domain waveforms and corresponding spectra for both pump conditions were measured using home-made LabVIEW software. As shown in Fig. 6(a), the THz waveform generated by the 49 fs pulse is significantly narrower compared with the 200 fs pulse, indicating that shorter pump pulses result in more compact THz waveforms, thereby enhancing the time-domain resolution. Fig. 6(b) compares the spectral characteristics: the 200 fs pulse generates THz radiation with a center frequency of around 0.5 THz and a cutoff frequency near 2 THz, while the 49 fs pulse produces a higher center frequency of approximately 0.84 THz and a broader bandwidth extending up to 4.1 THz. It should be noted that, in EO sampling, the use of 200 fs probe pulses and a 2-mm-thick GaP crystal imposes a bandwidth limitation on the detected THz spectrum. Consequently, the actual THz spectrum may be broader than what is presented in Fig. 6, particularly in the case of the 49 fs pump pulse. This detection constraint should be taken into account when interpreting the measured spectral bandwidth.

Although the shorter 49 fs pulse generates a broader THz spectrum, it comes at the cost of lower THz output power and field strength compared with the longer 200 fs pulse. This tradeoff between spectral width and conversion efficiency is a crucial aspect of the study. Despite the lower THz power, the broader spectral bandwidth enhances time-domain resolution and frequency coverage, which are particularly important for THz-STM. The THz output power was measured near the focal point of the THz beam using a calibrated THz power meter (THZ5B-BL-DZ-D0, Gentec-EO). The measurements were conducted under identical pump conditions (13.5 W at 520.8 kHz) for both cases. For a 200 fs pump pulse, the generated THz power was 1.56 mW, whereas for a 49 fs pump pulse, it was 0.15 mW. The power meter was positioned to capture the peak THz intensity at the focus, and appropriate alignment was ensured to minimize measurement uncertainties. Correspondingly, the conversion efficiency of THz generation was calculated as 1.11×10^{-5} for the 49 fs pulse and 1.15×10^{-4} for the 200 fs pulse. Even though the 49 fs pulse produces much lower THz energy, it is still stronger than other THz sources used in THz-STM systems, e.g., photon-conducive antenna THz source [42], and is sufficient for THz-STM applications.

In summary, a broader-bandwidth THz radiation output has been achieved in the higher repetition rate $LiNbO_3$ THz source, while its power level meets the requirements for integration into STM applications. These findings demonstrate the significant role of pulse duration in optimizing the performance of $LiNbO_3$-based THz sources. The 49 fs pulse, achieved through MPC compression, significantly broadens the THz spectrum, which is critical for optimizing high-frequency broadband THz sources, especially for advancing THz-STM technology.

IV. Conclusion

This study demonstrates the successful application of a single-stage MPC nonlinear compression system to compress high-repetition-rate (520.8 kHz) 1030 nm laser pulses from 200 to 49 fs. The compressed pulses were used to generate broadband THz radiation in a 0.6% MgO-doped stoichiometric $LiNbO_3$ crystal, resulting in a THz source with a center frequency of 0.84 THz and a cutoff frequency of 4.1 THz. The results show that shorter pulses (49 fs) significantly broaden the THz spectrum, enhancing the spectral bandwidth from 0.5 to 0.84 THz and extending the cutoff frequency from 2 to 4.1 THz. While narrower pulses increase bandwidth, they come at the cost of lower conversion efficiency and reduced output power compared with longer pulses. However, the broader THz spectrum generated by shorter pulses is critical for improving THz-STM temporal resolution, which is limited in current $LiNbO_3$-based THz-STM systems. Due to the difficulty of coupling and the stability problem for the whole system, this study has not directly integrated the broadband THz source with THz-STM for experimental verification. However, it is expected that this new strategy for generating broadband $LiNbO_3$ THz sources will significantly enhance the potential application of THz-STM in material analysis and nanoscale imaging.

The enhanced time-domain resolution and frequency coverage achieved with the shorter pulses pave the way for new possibilities in high-resolution imaging and material analysis, particularly in THz-STM. These improvements are essential for the accurate characterization of nanomaterials and complex samples. This work highlights the potential of MPC compression technology to significantly improve THz bandwidth, enabling advanced applications in ultrafast optics, imaging, and THz-STM, particularly for nanoscale analysis and complex sample characterization.

Acknowledgment

The authors would like to thank T. Wang for his support.

References

[1] M. Liu et al., “Terahertz-field-induced insulator-to-metal transition in vanadium dioxide metamaterial,” *Nature*, vol. 487, no. 7407, pp. 345–348, Jul. 2012.

[2] H. A. Hafez et al., “Intense terahertz radiation and their applications,” *J. Opt.*, vol. 18, no. 9, Sep. 2016, Art. no. 093004.

[3] H. A. Hafez et al., “Extremely efficient terahertz high-harmonic generation in graphene by hot Dirac fermions,” *Nature*, vol. 561, no. 7724, pp. 507–511, Sep. 2018.

[4] H. Li et al., “Unveiling nanoscale THz-STM imaging techniques on graphene nanoribbons with zigzag edge topology,” *Opt. Exp.*, vol. 32, no. 18, pp. 32062–32078, Sep. 2024.

[5] T. Kampfrath, K. Tanaka, and K. A. Nelson, “Resonant and nonresonant control over matter and light by intense terahertz transients,” *Nature Photon.*, vol. 7, no. 9, pp. 680–690, Sep. 2013.

[6] X. Miao, H. Zhan, and K. Zhao, “Application of THz technology in oil and gas optics,” *Sci. China Phys. Mech. Astron.*, vol. 60, no. 2, Feb. 2017, Art. no. 024231.

[7] H. Y. Hwang et al., “A review of non-linear terahertz spectroscopy with ultrashort tabletop-laser pulses,” *J. Mod. Opt.*, vol. 62, no. 18, pp. 1447–1479, Oct. 2015.

[8] G. Tóth, G. Polónyi, and J. Hebling, “Tilted pulse front pumping techniques for efficient terahertz pulse generation,” *Light, Sci. Appl.*, vol. 12, no. 1, Oct. 2023, Art. no. 256.

[9] L. Wang, G. Toth, J. Hebling, and F. Kartner, “Tilted-pulse-front schemes for terahertz generation,” *Laser Photon. Rev.*, vol. 14, no. 7, Jul. 2020, Art. no. 2000021.

[10] M. Arrigoni, S. Butcher, and J. Henrich, “Ultrafast lasers: Trends in femtosecond amplifiers—Ti: Sapphire vs. ytterbium,” *Laser Focus World*, vol. 56, no. 1, pp. 1–7, Jan. 2020.

[11] P. S. Nugraha et al., “Demonstration of a tilted-pulse-front pumped plane-parallel slab terahertz source,” *Opt. Lett.*, vol. 44, no. 4, pp. 1023–1026, Feb. 2019.

[12] B. Zhang et al., “1.4-mJ high energy terahertz radiation from lithium niobates,” *Laser Photon. Rev.*, vol. 15, no. 3, Mar. 2021, Art. no. 2000295.

[13] P. Russbueldt, T. Mans, J. Weitenberg, H. D. Hoffmann, and R. Poprawe, “Compact diode-pumped 1.1 kW Yb: YAG Innoslab femtosecond amplifier,” *Opt. Lett.*, vol. 35, no. 24, pp. 4169–4171, Dec. 2010.

[14] F. Meyer et al., “Milliwatt-class broadband THz source driven by a 112 W, sub-100 fs thin-disk laser,” *Opt. Exp.*, vol. 27, no. 21, pp. 30340–30349, Oct. 2019.

[15] Y. Ochi et al., “Yb:YAG thin-disk chirped pulse amplification laser system for intense terahertz pulse generation,” *Opt. Exp.*, vol. 23, no. 11, pp. 15057–15064, Jun. 2015.

[16] M. Tani, M. Herrmann, and K. Sakai, “Generation and detection of terahertz pulsed radiation with photoconductive antennas and its application to imaging,” *Meas. Sci. Technol.*, vol. 13, no. 11, pp. 1739–1745, 2002.

[17] S. Wang and X. C. Zhang, “Pulsed terahertz tomography,” *J. Phys. D, Appl. Phys.*, vol. 37, no. 4, pp. R1–R36, 2004.

[18] M. Zhai, A. Locquet, and D. S. Citrin, “Pulsed THz imaging for thickness characterization of plastic sheets,” *NDT E Int.*, vol. 116, 2020, Art. no. 102338.

[19] A. J. Huber, F. Keilmann, J. Wittborn, J. Aizpurua, and R. Hillenbrand, “Terahertz near-field nanoscopy of mobile carriers in single semiconductor nanodevices,” *Nano Lett.*, vol. 8, no. 11, pp. 3766–3770, Nov. 2008.

[20] T. Neuman et al., “Mapping the near fields of plasmonic nanoantennas by scattering-type scanning near-field optical microscopy,” *Laser Photon. Rev.*, vol. 9, no. 6, pp. 637–649, 2015.

[21] L. Wang, Y. Xia, and W. Ho, “Atomic-scale quantum sensing based on the ultrafast coherence of an H_2 molecule in an STM cavity,” *Science*, vol. 376, no. 6591, pp. 401–405, Apr. 2022.

[22] J. A. Fülöp et al., “Efficient generation of THz pulses with 0.4 mJ energy,” *Opt. Exp.*, vol. 22, no. 17, pp. 20155–20163, Aug. 2014.

[23] W. Schneider et al., “800 fs, 330-μJ pulses from a 100-W regenerative Yb:YAG thin-disk amplifier at 300 kHz and THz generation in $LiNbO_3$,” *Opt. Lett.*, vol. 39, no. 23, pp. 6604–6607, Dec. 2014.

[24] P. L. Kramer et al., "Enabling high repetition rate nonlinear THz science with a kilowatt-class sub-100 fs laser source," *Opt. Exp.*, vol. 28, no. 11, pp. 16951–16967, May 2020.
[25] F. Meyer, T. Vogel, S. Ahmed, and C. J. Saraceno, "Single-cycle, MHz repetition rate THz source with 66 mW of average power," *Opt. Lett.*, vol. 45, no. 9, pp. 2494–2497, May 2020.
[26] T. L. Cocker et al., "An ultrafast terahertz scanning tunnelling microscope," *Nature Photon.*, vol. 7, no. 8, pp. 620–625, Aug. 2013.
[27] C. Roelcke et al., "Ultrafast atomic-scale scanning tunnelling spectroscopy of a single vacancy in a monolayer crystal," *Nature Photon.*, vol. 18, pp. 595–602, 2024.
[28] J. Allerbeck et al., "Efficient and continuous carrier-envelope phase control for terahertz lightwave-driven scanning probe microscopy," *ACS Photon.*, vol. 10, no. 11, pp. 3888–3895, Nov. 2023.
[29] M. Abdo et al., "Variable repetition rate THz source for ultrafast scanning tunneling microscopy," *ACS Photon.*, vol. 8, no. 3, pp. 702–708, Mar. 2021.
[30] S. E. Ammerman et al., "Lightwave-driven scanning tunnelling spectroscopy of atomically precise graphene nanoribbons," *Nature Commun.*, vol. 12, no. 1, Jan. 2021, Art. no. 6794.
[31] K. Kimura et al., "Terahertz-field-driven scanning tunneling luminescence spectroscopy," *ACS Photon.*, vol. 8, no. 4, pp. 982–987, Apr. 2021.
[32] V. Jelic et al., "Atomic-scale terahertz time-domain spectroscopy," *Nature Photon.*, vol. 18, no. 9, pp. 898–904, Sep. 2024.
[33] H. Li et al., "Real-space sampling of terahertz waveforms under scanning tunneling microscope," *ACS Photon.*, vol. 11, no. 4, pp. 1428–1437, Apr. 2024.
[34] T. Tachizaki et al., "On the progress of ultrafast time-resolved THz scanning tunneling microscopy," *APL Mater.*, vol. 9, no. 6, Jun. 2021, Art. no. 060903.
[35] J. Schulte et al., "Nonlinear pulse compression in a multi-pass cell," *Opt. Lett.*, vol. 41, no. 19, pp. 4511–4514, Oct. 2016.
[36] S. Zhang et al., "Solitary beam propagation in periodic layered Kerr media enables high-efficiency pulse compression and mode self-cleaning," *Light, Sci. Appl.*, vol. 10, no. 1, Jan. 2021, Art. no. 53.
[37] J. Weitenberg et al., "Multi-pass-cell-based nonlinear pulse compression to 115 fs at 7.5 µj pulse energy and 300 W average power," *Opt. Exp.*, vol. 25, no. 17, pp. 20502–20510, Aug. 2017.
[38] A. L. Viotti et al., "Multi-pass cells for post-compression of ultrashort laser pulses," *Optica*, vol. 9, no. 2, pp. 197–216, Feb. 2022.
[39] C. M. Heyl et al., "High-energy bow tie multi-pass cells for nonlinear spectral broadening applications," *J. Phys., Photon.*, vol. 4, no. 1, Jan. 2022, Art. no. 014002.
[40] H. Hirori, F. Blanchard, and K. Tanaka, "Single-cycle terahertz pulses with amplitudes exceeding 1 MV/cm generated by optical rectification in $LiNbO_3$," *Appl. Phys. Lett.*, vol. 98, no. 9, Feb. 2011, Art. no. 091106.
[41] K. Ravi et al., "Theory of terahertz generation by optical rectification using tilted-pulse-fronts," *Opt. Exp.*, vol. 23, no. 4, pp. 5253–5276, Feb. 2015.
[42] H. Azazoglu et al., "Variable-temperature lightwave-driven scanning tunneling microscope with a compact, turn-key terahertz source," *Rev. Sci. Instrum.*, vol. 95, no. 2, Feb. 2024, Art. no. 023703.

Lu-Zhen Chen was born in Hainan, China, on April 18, 1995. He received the B.S. degree in electronic information science and technology in 2020 from Hainan Normal University, Haikou, China, where he is currently working toward the master's degree in optoelectronic information engineering with joint training with the Guangdong Provincial Key Laboratory of Terahertz Quantum Electromagnetics, Guangzhou, China.

His current research involves ultrafast optics and terahertz source generation.

Hong-Bo Li was born in Sichuan, China, on September 6, 1998. He received the B.S. degree in physics and electronics and information engineering in 2020 from the University of Chinese Academy of Science, Beijing, China, where he is currently working toward the Ph.D. degree in electromagneticfield and microwave technology with the Guangdong Key Laboratory of Terahertz Quantum Electromagnetism.

His current research involves ultrafast terahertz scanning microscopy.

Dong-Liang Xie, photograph and biography not available at the time of publication.

Kai Zhang, photograph and biography not available at the time of publication.

Jing-Yin Xu, photograph and biography not available at the time of publication.

Hao-Ran Song, photograph and biography not available at the time of publication.

Hong Li, photograph and biography not available at the time of publication.

Tian-Wu Wang was born in Heilongjiang, China. He received the Ph.D. degree in terahertz time-domain spectroscopy from the Technical University of Denmark, Kongens Lyngby, Denmark, in 2015.

After that, he was a Postdoctoral Researcher with the University of Alberta, Canada. In 2020, he became an Associate Researcher with Aerospace Information Research Institute, Chinese Academy of Sciences (CAS). In 2023, he was promoted to Researcher with Aerospace Information Research Institute, CAS. His current research interests include time-resolved terahertz time-domain spectroscopy, terahertz near-field imaging, terahertz generation and detection techniques, and ultrafast dynamics of low-dimensional materials.

Yi Qu was born in Jilin, China. He received the Ph.D. degree in microelectronics andsolid state electronics from Jilin University, Changchun, China, in 2002.

In 2003, he was appointed as a Professor with the National Key Laboratory of High-Power Semiconductor Laser, Changchun University of Science and Technology. From 2003 to 2005, he was a Postdoctoral Research Fellow with the School of Materials Engineering, Nanyang Technological University, Singapore. From 2006 to 2017, he served as the Deputy Director of the National Key Laboratory of High-Power Semiconductor Laser, Changchun University of Science and Technology. In 2012, he was a Senior Research Scholar with the Department of Electrical Engineering, Yale University, USA, where he visited for academic collaboration from February to August 2012. In 2017, he became the Director of the Hainan Province Key Laboratory of Laser Technology and Optoelectronic Functional Materials. His current research interests include terahertz emission, various novel semiconductor lasers (such as 4–6 μm/8–12 μm quantum cascade laser chip fabrication and packaging and monolithic dual-wavelength semiconductor lasers), micro/nanosatellite laser communication systems, and semiconductor laser radar.